



Since January 2020 Elsevier has created a COVID-19 resource centre with free information in English and Mandarin on the novel coronavirus COVID-19. The COVID-19 resource centre is hosted on Elsevier Connect, the company's public news and information website.

Elsevier hereby grants permission to make all its COVID-19-related research that is available on the COVID-19 resource centre - including this research content - immediately available in PubMed Central and other publicly funded repositories, such as the WHO COVID database with rights for unrestricted research re-use and analyses in any form or by any means with acknowledgement of the original source. These permissions are granted for free by Elsevier for as long as the COVID-19 resource centre remains active.



# Nitrogen-rich based conjugated microporous polymers for highly efficient adsorption and removal of COVID-19 antiviral drug chloroquine phosphate from environmental waters

Xiao-Xing Wang<sup>a,b</sup>, Lu Liu<sup>a,\*</sup>, Qi-Feng Li<sup>c</sup>, Hua Xiao<sup>a</sup>, Ming-Lin Wang<sup>b</sup>, Hai-Chen Tu<sup>a</sup>, Jin-Ming Lin<sup>d</sup>, Ru-Song Zhao<sup>a,\*</sup>

<sup>a</sup> Qilu University of Technology (Shandong Academy of Sciences), Shandong Analysis and Test Center, Key Laboratory for Applied Technology of Sophisticated Analytical Instruments of Shandong Province, Jinan 250014, China

<sup>b</sup> College of Food Science and Engineering, Shandong Agricultural University, Taian 271018, China

<sup>c</sup> Department of Pharmaceutical Engineering, Shandong Medicine Technician College, Taian 271000, China

<sup>d</sup> Department of Chemistry, Tsinghua University, Beijing 100084, China

## ARTICLE INFO

### Keywords:

Conjugated microporous polymers  
Removal  
Adsorption  
Chloroquine phosphate

## ABSTRACT

Chloroquine phosphate (CQP) has been suggested as an important and effective clinical reliever medication for the 2019 coronavirus (COVID-19). Nevertheless, its excessive use will inevitably cause irreparable damage to the entire ecosystem, thereby posing a considerable environmental safety concern. Hence, the development of highly-efficient methods of removing CQP from water pollution sources, e.g., effluents from hospitals and pharmaceutical factories is significant. This study reported the fabrication of novel C–N bond linked conjugated microporous polymers (CMPs) (BPT–DMB–CMP) with multiple nitrogen-rich anchoring sites for the quick and efficient removal of CQP from aqueous solutions. The irreversible covalent C–N bond linked in the internal framework of BPT–DMB–CMP endowed it with good chemical stability and excellent adsorbent regeneration. With its pre-designed functional groups (i.e., rich N–H bonds, triazine rings, and benzene rings) and large area surface (1,019.89 m<sup>2</sup>·g<sup>-1</sup>), BPT–DMB–CMP demonstrated rapid adsorption kinetics (25 min) and an extraordinary adsorption capacity (334.70 mg·g<sup>-1</sup>) for CQP, which is relatively higher than that of other adsorbents. The adsorption behavior of CQP on BPT–DMB–CMP corresponded with Liu model and mixed-order model. Based on the density functional theory (DFT) calculations, X-ray photoelectron spectroscopy (XPS), and adsorption comparisons test, the halogen bonding, and hydrogen bonding cooperates with  $\pi-\pi$ , C–H $\cdots\pi$  interactions and size-matching effect in the CQP adsorption system on BPT–DMB–CMP. The excellent practicability for the removal of CQP from real wastewater samples verified the prospect of practical application of BPT–DMB–CMP. BPT–DMB–CMP exhibited the application potentials for the adsorption of other antiviral drugs. This work opens up an efficient, simple, and high adsorption capacity way for removal CQP.

## 1. Introduction

Chloroquine phosphate (CQP), the chemical name of 7-chloro-4-(4-diethylamino-1-methylbutylamino) quinoline, has been shown to be a safe and efficient drug for the treatment of malaria and autoimmune diseases [1]. In 2020, CQP was thrust into the limelight due to its effective inhibition of the 2019 coronavirus (COVID-19) caused by the SARS-CoV-2 virus [2–5]. With persistent and global presence of COVID-19, CQP, as one of the emerging contaminants (ECs), its large-scale use and bio-accumulation could accelerate the proliferation of chloroquine-

resistant strains of plasmodium species in the eco-environment, which could disrupt the entire ecological balance and threaten the health of living beings [6–8]. As the only water treatment method currently available, degradation has been used to treat CQP from water system as far as we know. For instance, degradation methods using PDINH/MIL-88A(Fe) [9], BUC-21(Fe) composites [10], SA Co–N–C (30)/PMS [11] system, and Co–Mg mixed metal oxides [12], were developed for CQP removal, respectively. However, the degradation process is often complex, moreover, it can produce some low molecular compounds. Accordingly, exploring a highly effective and simple water treatment

\* Corresponding authors.

E-mail addresses: [15966632980@163.com](mailto:15966632980@163.com) (L. Liu), [zhaors1976@126.com](mailto:zhaors1976@126.com) (R.-S. Zhao).

<https://doi.org/10.1016/j.seppur.2022.122517>

Received 21 September 2022; Received in revised form 26 October 2022; Accepted 27 October 2022

Available online 1 November 2022

1383-5866/© 2022 Elsevier B.V. All rights reserved.

process to remove CQP residue is of paramount importance.

Adsorption is an effective physical removal method, which has been broadly applied for the elimination of organic pollutants from various matrixes due to it being simple, efficiency, cost-effective, and environmentally friendly [13–19]. However, highly efficient adsorption technology requires an excellent adsorbent. Many types of adsorbents have been utilized to adsorption, including carbon nanotubes [20], layered double hydroxides [21], covalent organic frameworks [22], and biochar [23]. At the same time, advanced materials with high capacity, outstanding adsorption efficiency, and excellent regeneration have always garnered substantial attention as adsorbents and have been the focus by researchers.

Conjugated microporous polymers (CMPs) [24–27] are a type of polymer with a pore size smaller than 2 nm. They are assembled into rich  $\pi$ -conjugated backbones via irreversible covalent bonds, and possess outstanding and inherent properties, including adjustable structure and pore size, excellent stabilities, and large surface area [28–30]. Therefore, when used as adsorbents, CMPs could provide high adsorptive capacity or ultra-sensitivity in the fields of enrichment and removal of contaminants. Different polymerization methods, including Suzuki coupling [31], Heck coupling [32], Sonogashira coupling [33], Buchwald-Hartwig (BH) coupling and so on, have been used to construct various CMPs. For instance, BH coupling was used to produce three-dimensional analogues via common amination reactions, which were triggered via palladium-catalyzed coupling between amines and aryl bromides [34,35]. As the simple approach of expansion of C–N bonds [36,37], CMPs obtained by BH coupling possessed bonding with CQP. Furthermore, an abundant  $\pi$ -conjugated structure with specific electron-donating idiosyncrasy could strengthen the  $\pi$ – $\pi$  stacking interaction with the benzene rings of CQP [38]. The above-formed interactions could provide BH-prepared CMPs with significant potential to improve their adsorption capacity and rate for CQP.

Herein, a stable CMP with high surface area was prepared from 2, 4, 6-Tris(4-bromophenyl)-1, 3, 5-triazine (BPT) and 2, 2-Dimethyl-(1, 1-biphenyl)-4, 4-diamine (DMB) (BPT–DMB–CMP) via BH coupling (Scheme 1), which was an adsorbent worked for the rapid adsorption and effective removal of CQP from aqueous solutions. The triazine groups were selected and decorated within the BPT–DMB–CMP framework to enhance internal stability and provide multitudinous N-rich functional sites to realize excellent removal performance via potential halogen-bonding interaction. The optimized BH cross-coupling strategy for fabricating the BPT–DMB–CMP provided a relatively large surface area and excellent chemical stability. The influence of adsorption (pH and adsorbent dosage) was explored and optimized in detail. The adsorption kinetics, adsorption isotherms, and thermodynamics of BPT–DMB–CMP for the removal of CQP were explored in depth. Exploiting the abundant aromatic rings, triazine rings and the expansion of C–N bonds by BH coupling, the prepared BPT–DMB–CMP exhibited outstanding adsorption capacity and rate to CQP via the designed pivotal roles, *i.e.*, halogen bonding, hydrogen bonding,  $\pi$ – $\pi$  interaction, C–H $\cdots$  $\pi$  interaction, and size matching effect, which was tested and simulated by X-ray photoelectron spectroscopy (XPS), density functional theory (DFT) calculation, and adsorption test. The excellent adsorption

performance of BPT–DMB–CMP promoted the successful application of the removal for CQP from three real wastewater samples (pharmaceutical factories effluents, pool water, and underground water). Additionally, the adsorption capacities for other antiviral drugs on BPT–DMB–CMP in single and mixed systems were explored. This present work provides a novel, highly efficient, and simple method for removal of CQP based on BPT–DMB–CMP in water treatment process.

## 2. Materials and methods

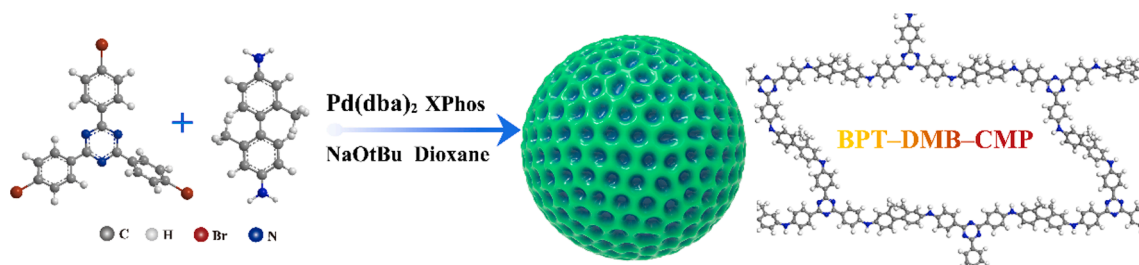
### 2.1. Chemicals and characterization

The DMB, BPT, 1, 3, 5-Tris (4-bromophenyl) benzene (TBB), 4, 4'-biphenylenediamine (BPDA), and Bis(dibenzylideneacetone)palladium ( $\text{Pd}(\text{dba})_2$ ) used in this study were from the Aladdin Biochemical Technology Co., Ltd. (Shanghai, China). 2-(Dicyclohexylphosphino)-2, 4, 6-tri-*i*-propyl-1, 1-biphen (XPhos) was obtained from the Alfa Chemical Co., Ltd. (Zhengzhou, China). CQP, famciclovir, lamivudine, and favipiravir were provided by ANPEL Laboratory Technologies (Shanghai, China). Sodium *tert*-butoxide ( $\text{NaOtBu}$ ) was supplied by the Sinopharm Chemical Reagent Co., Ltd (Shanghai, China).

Scanning electron microscopy (SEM) images were studied using a German Zeiss SUPRA<sup>TM</sup>55 SEM instrument. A high vacuum with a 3 kV accelerating voltage was used for the SEM analysis. Fourier-transform infrared (FT-IR) spectroscopy was collected by a Nicolet 710 infrared (IR) spectrophotometer using wavenumbers ( $\text{cm}^{-1}$ ) to record the signal's transmittance (%). The gas adsorption–desorption experiments were recorded using a JW-BK300C volumetric sorption analyzer recorded and were conducted using ultra-high-purity  $\text{N}_2$  gases for the gas adsorption–desorption process. The XPS spectra were recorded on a Thermo Fisher Escalab 250xi instrument equipped with an Al monochromatic X-ray source. A BRUKER 400 MHz nuclear magnetic resonance (NMR) spectrometer recorded the Solid-state  $^{13}\text{C}$  NMR spectra. A Malvern Panalytical ZS90 instrument was used to obtain the zeta potential of BPT–DMB–CMP. Elemental combustion analysis has been performed on a UNICUBE elemental analyzer (Elementar Company, Germany). A Shimadzu UV2550 Ultraviolet–visible (UV–vis) spectrophotometer was used to record the UV–vis absorption spectra. The chromatographic for quantitative analysis of four antiviral drugs was conducted by the thermo U-3000 (Dionex, USA) system.

### 2.2. Synthesis of BPT–DMB–CMP

This study polymerized BPT–DMB–CMP in an optimized manner according to the previously reported methods [39] to provide a large specific surface area and a stable pore size. A round-bottomed flask was filled with BPT (273.03 mg, 0.5 mmol) as the core and DMB (70.05 mg, 0.33 mmol) as the linker, at a ratio of 1.5:1. Then  $\text{Pd}(\text{dba})_2$  (0.03 mmol), XPhos (0.045 mmol), and  $\text{NaOtBu}$  (3.5 mmol) were placed in the flask under an argon atmosphere to protect against the activation of the palladium catalyst. A 60-mL volume of dioxane was added to the mixture, which was heated to 85 °C and stirred under a magnetic force for 24 h. The obtained substance was washed separately once with



Scheme 1. Schematic illustration for the synthesis of BPT–DMB–CMP.

purified water and four times with methanol. Finally, the BPT–DMB–CMP was dried in a vacuum drying chamber at 60 °C for 12 h to obtain the final product in 83 % isolation yield. Elemental analysis (%) C, 73.01, H 4.90, N. 11.25. The two CMP without triazine groups (TBB–DMB–CMP and TBB–BPDA–CMP) were synthesized under the same condition via changing BPT (273.03 mg, 0.5 mmol) to TBB (271.54 mg, 0.5 mmol) and DMB (70.05 mg, 0.33 mmol) to BPDA (60.79 mg, 0.33 mmol), respectively.

### 2.3. Adsorption experiments

The CQP stocking solution concentration of 10,000 mg·L<sup>-1</sup> was prepared by adding a certain amount of CQP solid dissolving in pure water and storing it in a volumetric flask at 4 °C. The working solution was obtained by the stepwise thinning of the stocking solution. The pH of the working solution was 6.0.

**Adsorption kinetics:** An amount of (5.0 mg, 10.0 mg, and 20.0 mg) BPT–DMB–CMP were weighted and placed in a 40-mL headspace bottle with 10 mL of 100 mg·L<sup>-1</sup> CQP solution. The adsorbent concentration is referred to by  $C_s$ . At 35 °C, this mixture was agitated in an air bath thermostatic oscillator at a revolving speed of 260 rpm for different durations.

**Adsorption isotherms:** An amount of (5.0 mg, 10.0 mg, and 20.0 mg) BPT–DMB–CMP were weighted and placed in a 40-mL headspace bottle with 10 mL of CQP solution (the desired CQP concentration ranged 0–350 mg·L<sup>-1</sup>). The mixture was agitated in an air bath thermostatic oscillator at a revolving speed of 260 rpm under different temperatures (25 °C, 35 °C, and 45 °C) for 12 h.

Then, the separation of the supernatant from the solid phase was passed through a 0.45- $\mu$ m cellulose acetate filter. The obtained supernatant was thinned by pure water and explored by a UV–vis spectrophotometer. The wavelength was set at 343 nm for the detection of CQP. The term  $q_t$  (mg·g<sup>-1</sup>) refers to the adsorption capacity at time  $t$ , and  $q_e$  (mg·g<sup>-1</sup>) refers to the equilibrium adsorption capacity of equilibrium. These values were calculated using the following equations:

$$q_t = \frac{(C_0 - C_t)V}{m} \quad (1)$$

$$q_e = \frac{(C_0 - C_e)V}{m} \quad (2)$$

where  $C_0$ ,  $C_t$ , and  $C_e$  (all mg·L<sup>-1</sup>) refer to the concentration of CQP at initial,  $t$ , and equilibrium time, respectively. The term  $V$  (L) stands for the volume of the solution, and  $m$  (g) represents the BPT–DMB–CMP mass. The equations fitted by the adsorption isotherms and kinetic models can be found in the [Supporting Information](#).

### 2.4. Dft

The DFT calculations were used to simulate the elaborate adsorption mechanism from the adsorption process, which was accomplished using the Dmol<sup>3</sup> program package in Material studio. The exchange–correlation energy was calculated using the Perdew–Burke–Ernzerhof (PBE) function within the generalized gradient approximation (GGA). The  $c$ -axis of the one-layer-four-hole slab with a  $2 \times 2 \times 1$  BPT–DMB–CMP supercell was built to adsorb five identical CQP molecules. The guest molecular adsorption was analyzed using the Metropolis Monte Carlo algorithm.

### 2.5. Real water samples application

Pharmaceutical factories effluents and underground water were collected from Zhangqiu (Jinan, China). Pool water was collected from Jinan (China). The real samples were passed through a 0.45- $\mu$ m cellulose acetate filter. 5.0 mg of BPT–DMB–CMP was added into 10 mL of pharmaceutical factories effluents and underground water or pool water

with different spiked CQP solution (50 and 100 mg/L). The mixture was agitated in an air bath thermostatic oscillator at a revolving speed of 260 rpm at 35 °C for 12 h. The obtained supernatant was diluted by water and analyzed with UV–vis spectrophotometer.

## 3. Results and discussion

### 3.1. Characterization

The successful combination of the BPT–DMB–CMP network via BH coupling was verified by FT-IR spectra (Fig. 1A), solid <sup>13</sup>C NMR (Fig. 1B), and XPS spectra (Fig. 1C–E). The original characteristic peaks centered 3,337 cm<sup>-1</sup> and 3,397 cm<sup>-1</sup> correlating to the amine groups of DMB and the stretching vibrations at 1,171 cm<sup>-1</sup> and 1,009 cm<sup>-1</sup> arising from the aryl C–Br groups of BPT were diminished in the FT-IR spectrum of BPT–DMB–CMP, which indicated the occurrence of a complete polymerization reaction between the raw materials. However, after the BH coupling, newly characteristic peaks emerged at 1,078 cm<sup>-1</sup> and 816 cm<sup>-1</sup> from the C–N and C–H bonds. Moreover, the benzenoid-type secondary amine and aromatic rings at 1,598 cm<sup>-1</sup> and 1,502 cm<sup>-1</sup>, respectively, were clearly visible in the FT-IR spectra of the resulting CMP. Additionally, the triazine rings of the BPT stretching vibration at 1,365 cm<sup>-1</sup> remained in the BPT–DMB–CMP network. The solid <sup>13</sup>C NMR spectra exhibited a broadened chemical shift at approximately 118–143 ppm, which was caused by the substituted and unsubstituted phenyl carbons. Two additional resonances at approximately 24 ppm and 178 ppm were assigned to the methyl and triazine ring groups of BPT–DMB–CMP, respectively. The typical polyaniline XPS spectra shape was observed in the Fig. 1D, suggesting the polyaniline structure in the BPT–DMB–CMP network. The peak at binding energies of 399.06 eV for the N 1 s correspond to the –NH– bond derived from the BH coupling. The C 1 s peak at 286.22 eV and the N 1 s peak at 398.04 eV are indicative of the C=N bonds of triazine rings. The C 1 s peaks at 284.78 eV and 284.14 eV originated from the aromatic C and C–H bonds, respectively. All of the abovementioned charged chemical bonds are consistent with the predesigned architecture of BPT–DMB–CMP.

The morphological structure of BPT–DMB–CMP comprised abundant aggregated nanoparticles, as seen in the SEM image in Fig. 2A. Based on the International Union of Pure and Applied Chemistry's classification, the N<sub>2</sub> adsorption–desorption behavior of BPT–DMB–CMP (Fig. 2B and Fig. S1 and S2) belonged to Type I, reflecting the pore-filling phenomenon of a microporous adsorbent. It was noteworthy that the Brunauer–Emmett–Teller (BET) surface area of BPT–DMB–CMP reached up to 1,019.89 m<sup>2</sup>·g<sup>-1</sup>. The relatively large surface areas provided more adsorption spots to improve the CQP adsorption efficiency and rate of BPT–DMB–CMP. Calculated by Horvath–Kawazoe (HK) method, the dominant pore size distribution of BPT–DMB–CMP was located at 0.72 nm, as shown in Fig. 2B. The curve of the zeta potential of the BPT–DMB–CMP's surface ranged from pH 2.0 to 8.0, as plotted in Fig. 2C. The point of zero charge (pH<sub>pzc</sub>) of BPT–DMB–CMP was 5.0. The stability of BPT–DMB–CMP was confirmed by soaking in solutions of different polarities and pH levels for 72 h. The unchanged characteristic peak of the FT-IR spectra (Fig. 2D) confirmed the chemical stability of the intrinsic structure of BPT–DMB–CMP.

### 3.2. Factors affecting adsorption

To obtain the highest CQP removal efficiency rate, the adsorption conditions were optimized, including pH and adsorbent doses.

The pH value can substantially affect the surface charge properties of CQP and BPT–DMB–CMP, thereby influencing their interactions. Previous research results [9] revealed the pKa of CQP to be 8.4, which indicated that the CQP was in a cationic form at pH < 8.4. According to the results of the zeta potential of BPT–DMB–CMP, the negative charge of the surface of BPT–DMB–CMP promoted the adsorption process when pH > pH<sub>pzc</sub>. Hence, the highest removal efficiency of CQP occurred via

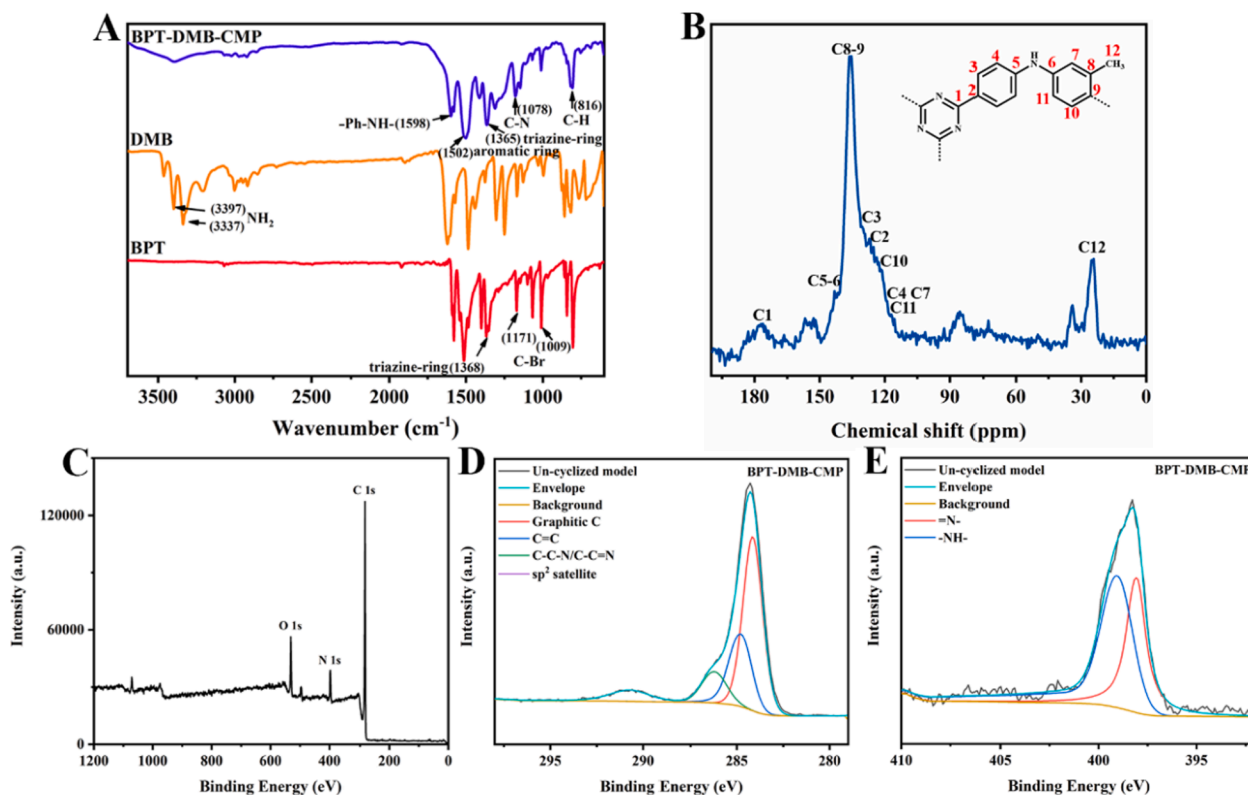


Fig. 1. (A) FT-IR spectra of BPT-DMB-CMP, (B) solid-state  $^{13}\text{C}$  NMR spectra of BPT-DMB-CMP, XPS spectra of BPT-DMB-CMP: (C) full scan, (D) N 1 s, (E) C 1 s.

electrostatic interaction at pH = 5.3–8.3. To further investigate the role of electrostatic interaction and achieve the highest CQP removal capacity by BPT-DMB-CMP, in a wide pH solution range (pH = 2.0–8.0), the  $q_m$  of the BPT-DMB-CMP for CQP was determined and analyzed, and the corresponding results are presented in Fig. 3A. The pH above 8.0 was not considered due to the instability of the CQP solution. The results revealed that the BPT-DMB-CMP exhibited  $q_m$  toward CQP when the pH was 6.0. At a pH level of 8.0, the number of positive charges of the CQP was significantly reduced (close to 0), and the electrostatic force was weak. Therefore, the high  $q_m$  was due to other possible interactions, such as  $\pi - \pi$  stacking, halogen bonding, and hydrogen bonding. A similar explanation could be applied to explain the slightly reduced  $q_m$  of BPT-DMB-CMP for CQP at pH = 4.0. When the pH was 2.0, a high electrostatic force decreased the removal capacity. These results indicate that electrostatic interaction was not dominant, whereas the combination of other possible  $\pi - \pi$  stacking, halogen bonding, and hydrogen bonding interactions would result in the enhanced extraction efficiency. Therefore, the optimal parameter was pH = 6.0.

The adsorption dosage of an adsorbent is a key indicator for assessing the highly efficient and economic removal of a contaminant. The  $q_e$  and removal efficiency in the CQP condition were evaluated by adding different BPT-DMB-CMP dosages to a 10-mL  $200 \text{ mg}\cdot\text{g}^{-1}$  CQP solution, as shown in Fig. 3B. As the mass of the BPT-DMB-CMP increased from 2.5 to 20.0 mg, there was a significant increase in the removal efficiency of CQP, which explained the increase in the free adsorption sites with the larger BPT-DMB-CMP mass. Conversely, the  $q_e$  of the BPT-DMB-CMP gradually decreased from  $250.54$  to  $80.83 \text{ mg}\cdot\text{g}^{-1}$ . This phenomenon could be because a lower unit weight of BPT-DMB-CMP is more likely to be fully exposed in the same CQP solution. The faster the saturation rate of the BPT-DMB-CMP adsorption site, the higher the  $q_e$  value. When the BPT-DMB-CMP dosage reached 5.0 mg, the increase in the adsorption efficiency rate began to decline, and the  $q_e$  value was relatively high. Considering the impact of economic effects, the optimum parameter for BPT-DMB-CMP was 5.0 mg.

### 3.3. Adsorption kinetics

Adsorption kinetics are the substantial description to elucidate the whole adsorption mass-transfer process and removal effectiveness for the establishment of a diffusion mechanism. To confirm the adsorption rate of CQP, the adsorption relationship between the contact time of BPT-DMB-CMP in a CQP aqueous solution and the adsorption capacity of BPT-DMB-CMP for CQP were determined and compared. Fig. S3 presents the adsorption kinetics of CQP on BPT-DMB-CMP for three different  $C_s$  (0.5, 1.0, and  $2.0 \text{ g}\cdot\text{L}^{-1}$ ). Between 80.38 % and 99.99 % of the CQP was removed at a low  $C_s$  (from 0.5 to  $2.0 \text{ g}\cdot\text{L}^{-1}$ ), which confirmed the high-adsorption capacity and excellent CQP removal efficiency of BPT-DMB-CMP. The equilibrium time of the CQP was realized within approximately 3 h for  $C_s$  of  $0.5 \text{ g}\cdot\text{L}^{-1}$ , 90 min for  $1.0 \text{ g}\cdot\text{L}^{-1}$ , and 25 min for  $2.0 \text{ g}\cdot\text{L}^{-1}$ , indicating the rapid removal of CQP by BPT-DMB-CMP.

Herein, pseudo-first-order (PFO) [Eq. (S4)] and pseudo-second-order (PSO) [Eq. (S5)] models were established to describe and fit the adsorption capacity at different times. A non-linear regression analysis and fitted parameters are shown in Fig. 4A and 4B, respectively, which were calculated by Eq. S4 and Eq. S5. The goodness of fit in terms of the coefficient of determination ( $R^2$ ) of the PFO model (0.9150, 0.9483, and 0.9939 for three different  $C_s$ ) and the PSO model (0.9705, 0.9904, and 0.9979) were all above 0.9000, which indicated that both pseudo models could adequately explain the adsorption of CQP. Hence, the mixed-order (MO) model, a general kinetic model containing PFO and PSO models, was applied to further describe this complex adsorption process. Fig. 4C and Table 1 present and summarize the graphical interpretation and fitting parameters of MO model, respectively, which were calculated by Eq. (S6). The good values of  $R^2$  (0.9705, 0.9904, and 0.9991) illustrated that the MO model well predicted the complex CQP adsorption process. The values of  $k_1'$  (0.00031, 0.0016, and 0.0556) and  $k_2'$  (0.00028, 0.00095, and 0.0074) confirmed that CQP adsorption was an interactive process involving both PFO and PSO kinetic processes

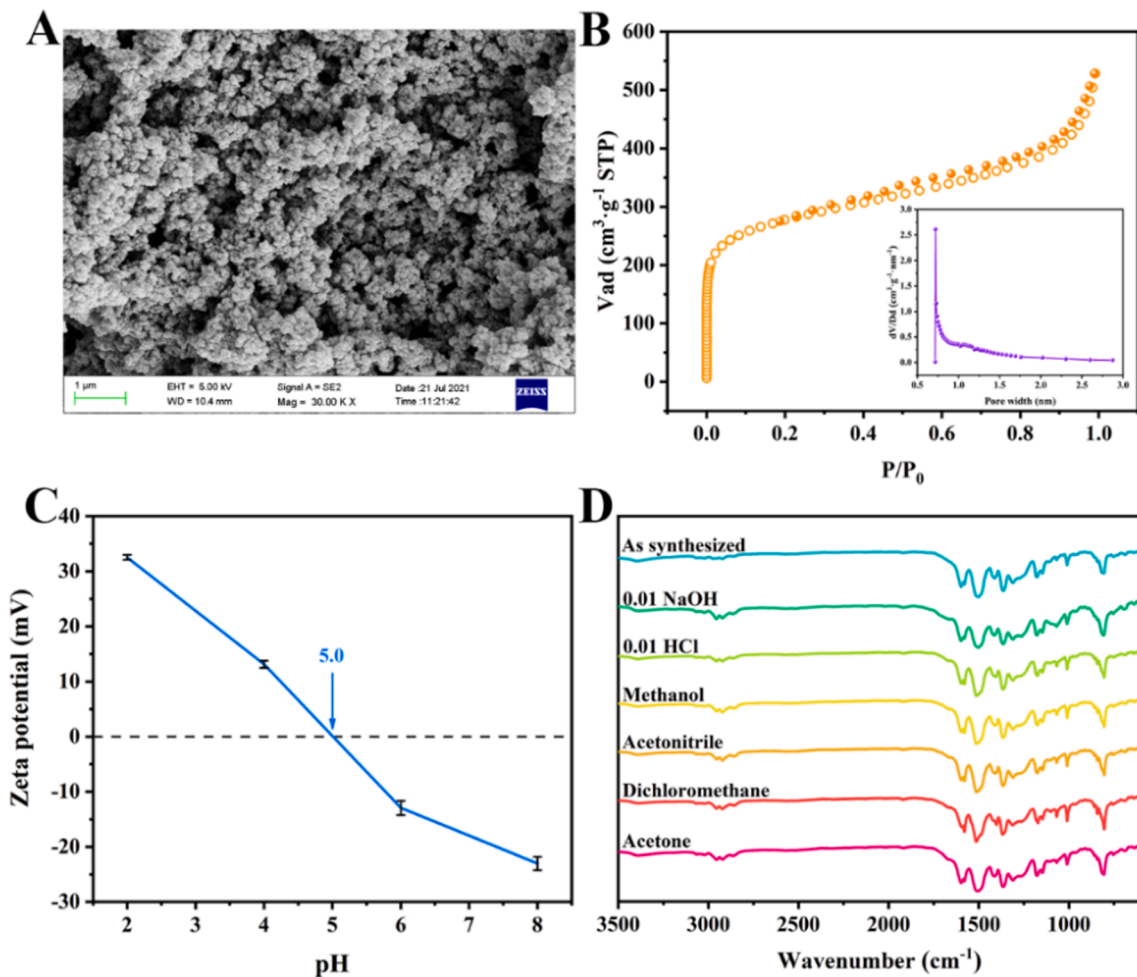


Fig. 2. (A) The SEM image, (B) N<sub>2</sub> adsorption–desorption isotherms and pore size distribution, (C) zeta potential, and (D) FT-IR spectra with treatment under various conditions of BPT–DMB–CMP.

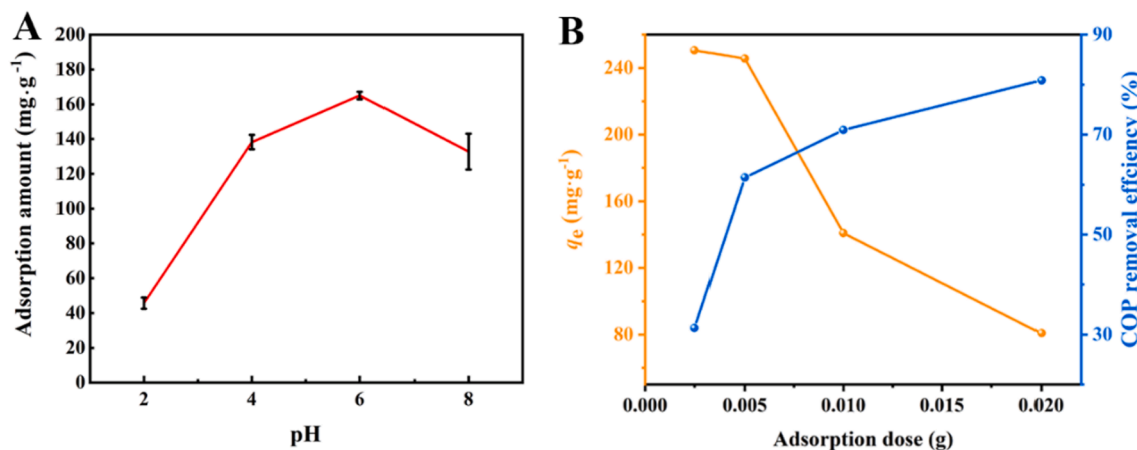


Fig. 3. Effects of (A) solution pH and (B) adsorbent dosage of CQP on BPT–DMB–CMP.

[22].

Fig. S4 showed the rate of the entire adsorption process of CQP at three different C<sub>s</sub>, which were calculated by Eq. (S1) and Eq. (S2). Other mass-transfer processes and the adsorption rates on the active sites were interpreted according to PFO and PSO rates, respectively. The rate of CQP removal continued to decline until the adsorption capacity reached the maximum, which revealed the gradual occupation and consumption

of adsorption sites by CQP diffusion with increasing contact time. The PSO rate was higher than that of PFO in the adsorption process of CQP onto BPT–DMB–CMP, indicating the active sites concerning adsorption rate was dominant rather than other mass-transfer processes. Hence, more active sites could be obtained via the functionalization of BPT–DMB–CMP, which provides more possibilities for higher adsorption capacities [40].

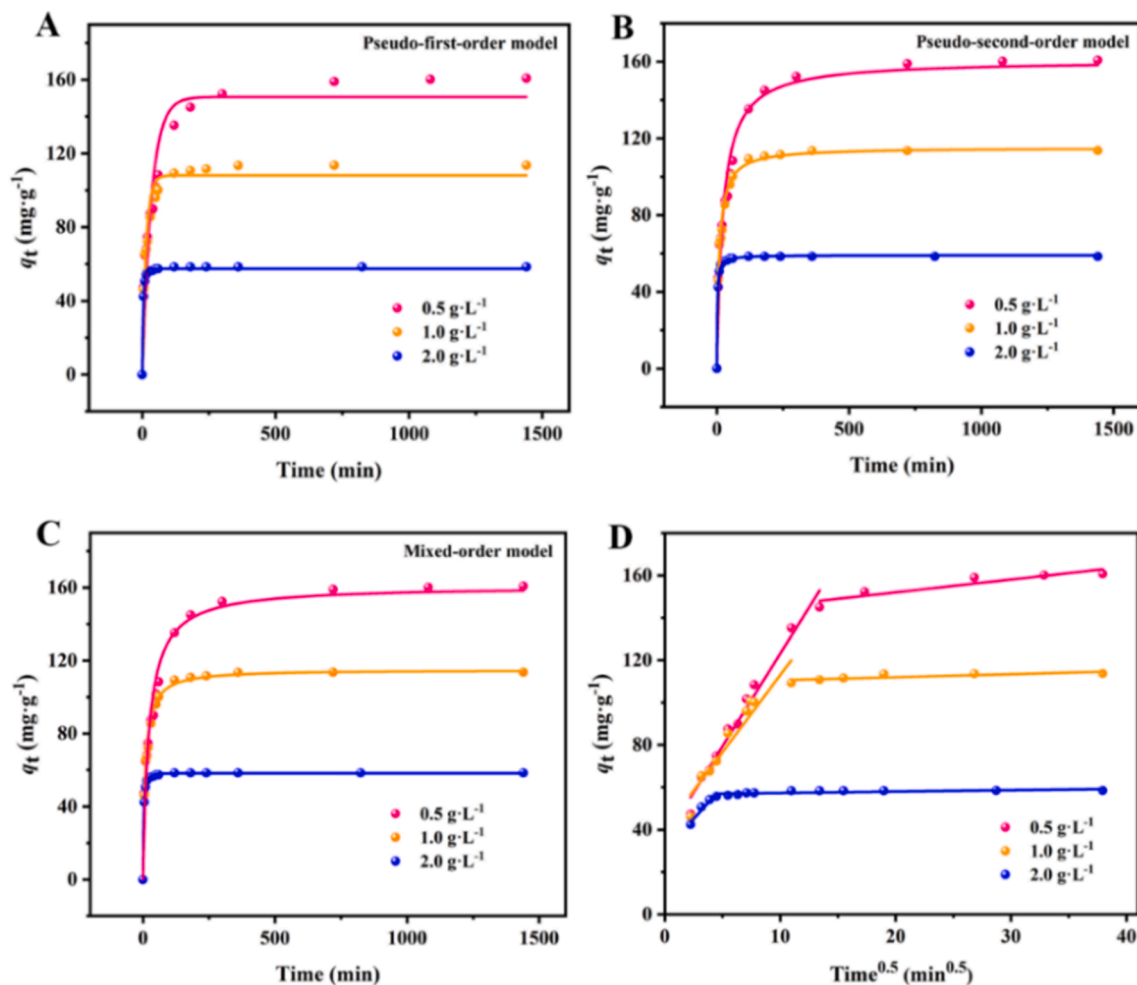


Fig. 4. The adsorption kinetics of CQP onto BPT-DMB-CMP fitted by (A) the PFO model, (B) PSO model, (C) MO model and (D) the intra-particle diffusion model.

Table 1  
Parameters of different kinetic models for CQP adsorption onto BPT-DMB-CMP.

Models	Parameters	$C_s$ (g·L <sup>-1</sup> )		
		0.5	1.0	2.0
PFO model	$k_1$ (min <sup>-1</sup> )	0.0292	0.0687	0.2468
	$q_e$ (mg·g <sup>-1</sup> )	150.65	108.06	57.44
	$R^2$	0.9150	0.9483	0.9939
PSO model	$k_2$ (g·mg <sup>-1</sup> ·min <sup>-1</sup> )	$2.7440 \times 10^{-4}$	$9.4926 \times 10^{-4}$	0.0097
	$q_e$ (mg·g <sup>-1</sup> )	160.73	115.21	59.12
	$R^2$	0.9705	0.9904	0.9979
MO model	$k_1'$ (min <sup>-1</sup> )	$3.0861 \times 10^{-4}$	0.0016	0.0556
	$k_2'$ (g·mg <sup>-1</sup> ·min <sup>-1</sup> )	$2.7383 \times 10^{-4}$	$9.5027 \times 10^{-4}$	0.0074
	$R^2$	0.9705	0.9904	0.9991

Confirming the potential rate-controlled steps of the adsorption process using only PFO, PSO, and MO models was difficult. Hence, intra-particle diffusion was considered to fit the obtained experimental results, which was calculated by Eq. (S7). From Fig. 4D, the straight regression line of  $q_t$  vs  $time^{1/2}$  did not pass through the origin, which implied that external mass transfer and intra-particle diffusion were controlled identically during the entire adsorption process [41].

### 3.4. Adsorption isotherms

Equilibrium adsorption isotherms allow the visualization of important information when investigating the  $q_m$  and explaining the

adsorption properties of an adsorbate bounding to the surface of an adsorbent.

The adsorption isotherms of CQP on BPT-DMB-CMP were investigated in three different experiments  $C_s$  (0.5, 1.0, and 2.0 g·L<sup>-1</sup>), and all data are plotted in Fig. 5A. The increase in the adsorption dosage caused the regular reduction of the  $q_m$  of BPT-DMB-CMP for CQP, which corresponds with the outcomes reported elsewhere [42]. In the present study, Langmuir [Eq. (S8)], Freundlich [Eq. (S9)], and Liu [Eq. (S10)] models were used to fit the given experimental data of CQP on BPT-DMB-CMP. The fitted curves and calculated parameters of these three isotherm models were presented in Fig. 5B–D, and Table 2, respectively.

The theoretical Langmuir model assumes that the adsorption process is monolayered with a homogenous surface and equivalent binding sites. The good values of  $K_L$  (0.0097–0.9093,  $0 < K_L < 1$ ) confirmed that the adsorption process for CQP was favorable for three given  $C_s$  [43]. The Freundlich model, an empirical equation, describes the assumption that all the active sites of an adsorbate are distributed on layers with a heterogenous surface and infinite adsorption possibilities. The values of  $n_F$  were between 1.7709 and 5.8207 ( $1 < n_F < 10$ ), which revealed that the removal process of CQP was both positive and spontaneous [44]. The Liu model is a formula derived from a combination of the Langmuir and Freundlich models, but discards the assumptions of the Langmuir model (i.e., the property of adsorption is monolayered) and the Freundlich model (i.e., infinite adsorption). Liu model assumes that the energy of different adsorption sites is diverse [21,45]. It can be clearly seen that, the  $R^2$  values of the Liu model (0.9660–0.9924) are close to 1.0, which

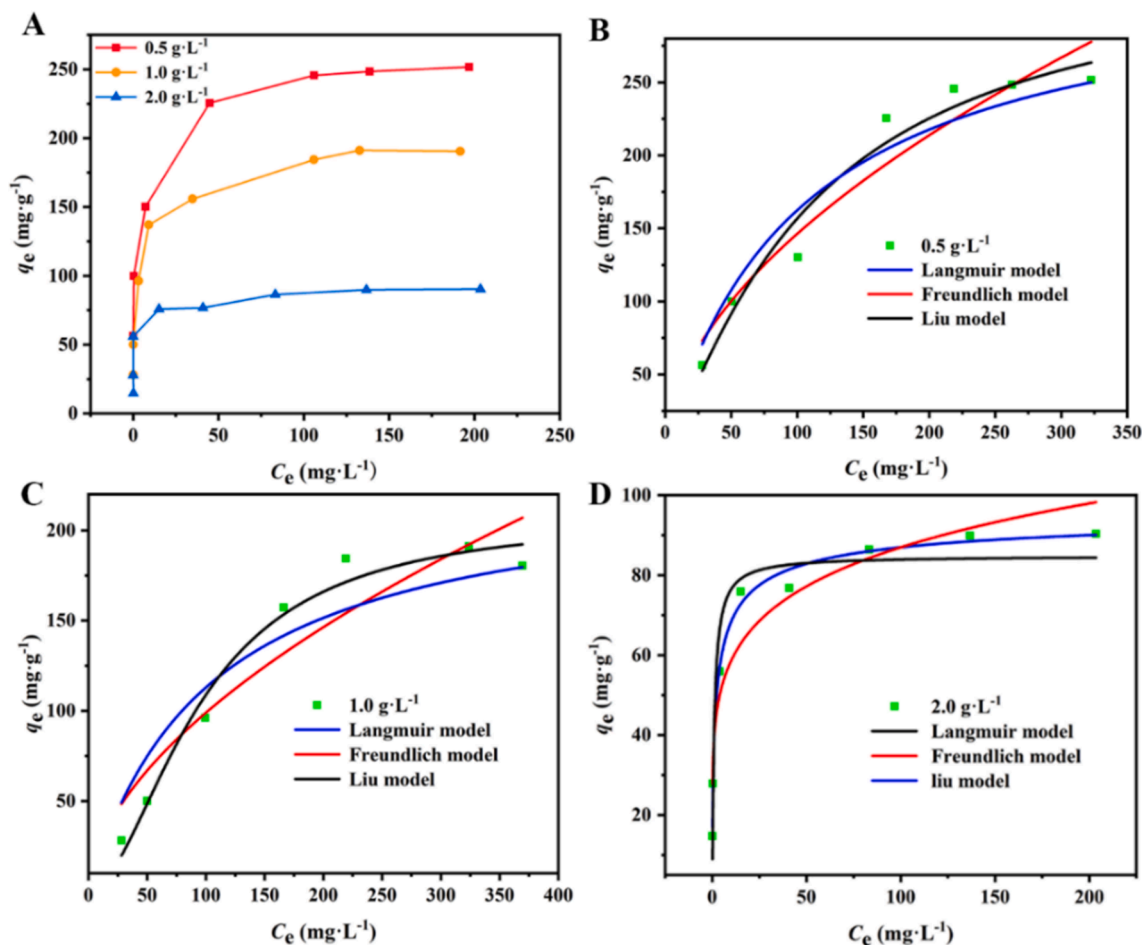


Fig. 5. (A) The adsorption isotherms CQP onto BPT-DMB-CMP, fitted by Langmuir model, Freundlich model and Liu model at (B) 0.5 g·L<sup>-1</sup>, (C) 1.0 g·L<sup>-1</sup>, (D) 2.0 g·L<sup>-1</sup>.

Table 2

Parameters of the Langmuir, Freundlich, and Liu models for the adsorption of CQP onto BPT-DMB-CMP at three different C<sub>s</sub>.

Equation	Parameter	C <sub>s</sub> (g·L <sup>-1</sup> )		
		0.5	1.0	2.0
Langmuir	q <sub>m</sub> (mg·g <sup>-1</sup> )	330.00	230.00	84.84
	K <sub>L</sub> (L·mg <sup>-1</sup> )	0.0097	0.0097	0.9093
	R <sup>2</sup>	0.9411	0.9047	0.9447
Freundlich	n <sub>F</sub>	1.8262	1.7709	5.8207
	K <sub>F</sub> [mg·g <sup>-1</sup> ·(mg·L <sup>-1</sup> ) <sup>-1/n<sub>F</sub></sup> ]	11.7474	7.3457	39.4491
	R <sup>2</sup>	0.9339	0.8935	0.9205
Liu	q <sub>m</sub> (mg·g <sup>-1</sup> )	334.70	207.80	97.24
	K <sub>g</sub> (L·mg <sup>-1</sup> )	0.0090	0.0105	0.4721
	n <sub>L</sub>	1.2272	1.8510	0.5544
	R <sup>2</sup>	0.9660	0.9804	0.9924

were higher than the Langmuir (0.9047–0.9447) and Freundlich (0.8935–0.9339) models. This indicated that the Liu model was preferable for visualizing the adsorption behavior of CQP on BPT-DMB-CMP. The remarkable q<sub>m</sub> obtained by the Liu model was 334.70 mg·g<sup>-1</sup> at a C<sub>s</sub> of 0.5 g·L<sup>-1</sup>.

The comparisons of CQP adsorption performance based on various reported adsorbents such as magnesium trisilicate [46], magnesium oxide [46], aluminium hydroxide [46], lantain peel activated carbon-supported zinc oxide (PPAC-ZnO) [47], hibiscus sabdariffa seed pods (HSP1) [48], agar-graphene oxide (A-GO) [49] and BPT-DMB-CMP are presented in Table 3. The q<sub>m</sub> of BPT-DMB-CMP is observed to maintain at a high level with value of 334.70 mg·g<sup>-1</sup>, which

Table 3

Comparison of CQP adsorption onto the reported various adsorbents.

Adsorbent	q <sub>m</sub> (mg·g <sup>-1</sup> )	Equilibrium time	Condition	Refs
Magnesium trisilicate	4.721	no given	T = 307 K	[46]
Magnesium oxide	4.175			
Aluminium hydroxide	3.911			
Edible clay	2.140			
PPAC-ZnO <sup>a</sup>	50.51	120 min	T = 313 K	[47]
HSP1 <sup>b</sup>	161.29	120 min	Cs = 0.08 g·L <sup>-1</sup> pH = 3.0 T = 328 K	[48]
A-GO <sup>c</sup>	63	no given	Cs = 0.02 g·L <sup>-1</sup> pH = 8.0 T = 297 K	[49]
BPT-DMB-CMP	334.70	25 min	Cs = 0.5 g·L <sup>-1</sup> pH = 6.0 T = 308 K	This work

PPAC-ZnO<sup>a</sup> = Plantain peel activated carbon-supported zinc oxide.

HSP1<sup>b</sup> = Hibiscus sabdariffa seed pods.

A-GO<sup>c</sup> = Agar-graphene oxide.

is relatively higher than that of other adsorbents. Additionally, the adsorption equilibrium time of CQP on BPT-DMB-CMP is advanced level (only 25 min), which is faster than that of the reported other materials. These comparisons indicated that BPT-DMB-CMP is a suitable adsorbent for the removal of CQP with high q<sub>m</sub> and fast adsorption rate.



### 3.5. Adsorption thermodynamics

The equilibrium adsorption isotherms of a range of temperature (25 °C–45 °C) of CQP on BPT–DMB–CMP were investigated (Fig. 6 and Table S1), and the corresponding fitted curves of the three models at different temperatures are presented in Fig. S5. A temperature of 35 °C provided the maximum adsorption capacity of BPT–DMB–CMP for CQP, indicating that high or low temperatures weaken the chelation between the adsorption sites of BPT–DMB–CMP and CQP, thereby reducing adsorption capacities.

To further investigate the energy changes of CQP adsorption onto BPT–DMB–CMP, we calculated the Gibbs free energy ( $\Delta G^\circ$ ), enthalpy change ( $\Delta H^\circ$ ), and entropy change ( $\Delta S^\circ$ ) values. These thermodynamic parameters for characterizing the adsorptive behavior were summarized and presented in Table 4. The thermodynamic equilibrium constant ( $K_e$ ) was acquired by the best fit model (the Liu model); this was calculated by the Liu model's constant ( $K_e$ ) value, which was changed from  $\text{L}\cdot\text{mg}^{-1}$  into  $\text{L}\cdot\text{mol}^{-1}$  [Eq. (S11)]. The Supporting Information contains the calculation formula and method. The spontaneous property of the adsorption of CQP onto BPT–DMB–CMP was obtained based on the negative  $\Delta G^\circ$  values ( $-5.13 \text{ kJ}\cdot\text{mol}^{-1}$  for 25 °C,  $-6.17 \text{ kJ}\cdot\text{mol}^{-1}$  for 35 °C, and  $-7.34 \text{ kJ}\cdot\text{mol}^{-1}$  for 45 °C), which were calculated based on Eq. (S12). Generally, the values of  $\Delta G^\circ$  ( $-20 \text{ kJ}\cdot\text{mol}^{-1} < \Delta G^\circ < 0 \text{ kJ}\cdot\text{mol}^{-1}$ ) were low for physisorption, whereas, the values of  $\Delta G^\circ$  ( $-800 \text{ kJ}\cdot\text{mol}^{-1} < \Delta G^\circ < -40 \text{ kJ}\cdot\text{mol}^{-1}$ ) were higher [50]. Hence, the physical adsorption between CQP and BPT–DMB–CMP was dominant. This phenomenon was further verified by  $\Delta H^\circ$ , which was calculated using Eq. (S13). The  $\Delta H^\circ$  value for physisorption was  $< 40 \text{ kJ}\cdot\text{mol}^{-1}$ , and the chemisorption value was between 40 and  $800 \text{ kJ}\cdot\text{mol}^{-1}$  [41]. The  $\Delta H^\circ$  value was  $20.12 \text{ kJ}\cdot\text{mol}^{-1}$ , which confirmed that the adoption was an endothermic reaction. The positive  $\Delta S^\circ$  of  $0.133 \text{ kJ}\cdot\text{mol}^{-1}\cdot\text{K}^{-1}$  hinted at an increase in the stochasticity of the solid–liquid border, indicating the excellent attraction between BPT–DMB–CMP and CQP.

### 3.6. Adsorption interaction mechanism

From the structural perspective, BPT–DMB–CMP are a type of rich  $\pi$ -conjugated backbone with triazine rings covalently linked by C–N bonds. Each triazine ring owns electropositive N atoms. Along with the large surface area of BPT–DMB–CMP, these functional groups contribute to CQP capture with their abundant aromatic rings and halogen atoms not only via hydrogen and halogen bonding but also by  $\pi$ - $\pi$  stacking interactions.

Firstly, the XPS characterizations of BPT–DMB–CMP before and after

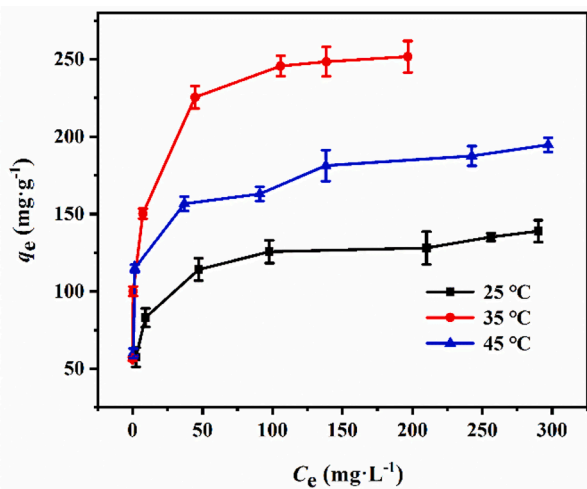


Fig. 6. The adsorption isotherms of CQP onto BPT–DMB–CMP at 25 °C, 35 °C, and 45 °C.

CQP adsorption were compared and analyzed to confirm the existence of the abovementioned interactions. Compared with the full scans of BPT–DMB–CMP and CQP (Fig. 7A and Fig. S6), a new characteristic peak ascribed to Cl 2p appeared after CQP adsorption. This result revealed only that CQP was captured onto BPT–DMB–CMP, but it did not prove that the interaction was due to halogen bonding. This is because the Cl...N interaction was too weak to be detected in the XPS spectrum [51]. Subsequently, DFT calculations were performed to confirm the existence of halogen bonding. Additionally, when CQP was adsorbed onto BPT–DMB–CMP, the C 1 s peak attributed to C=C bonds of BPT–DMB–CMP at binding energies of 284.68 eV moved to a relatively lower binding energy at 284.49 eV. Meanwhile, the C=C bonds content of BPT–DMB–CMP increased clearly from 26.11 % to 47.82 % after the extraction of CQP by BPT–DMB–CMP (Fig. 3D and 7B). The N 1 s peak located at 399.06 eV for –NH– were shifted to 399.44 eV after CQP adsorption (Fig. 3E and 7C). All these phenomena indicated the presence of both  $\pi$ - $\pi$  interaction and hydrogen bonding during the adsorption process in a real experimental environment [52,53].

From a molecular structure perspective, a DFT analysis was used to further confirm and reveal the interaction mechanism between CQP and BPT–DMB–CMP. Fig. 8A depicted the adsorption configuration of CQP adsorption on BPT–DMB–CMP. Fig. 8B and C demonstrate the possible C–H... $\pi$  stacking and  $\pi$ - $\pi$  stacking interactions. The strongly electropositive Cl element of CQP interacted with the N element, which possessed the electronegativity of the triazine ring of BPT–DMB–CMP, to produce halogen bonding, which is shown in Fig. 8D. The expansion of the C–N bonds of the BPT–DMB–CMP network facilitated the production of hydrogen bonding (Fig. 8E). Additionally, the BPT–DMB–CMP with large surface area ( $1,019.89 \text{ m}^2\cdot\text{g}^{-1}$ ) increased the adsorption sites and induced the occurrence of van der Waals (vdW) interactions. Based on the above analysis of potential mechanisms, the theoretical explanations were consistent with the experimental data in terms of the excellent CQP removal capacity of BPT–DMB–CMP.

In order to further prove the importance of N-rich material for improving the adsorption performance, by comparison, two CMP without triazine groups (TBB–DMB–CMP and TBB–BPDA–CMP) are designed and synthesized. The characterization data of TBB–DMB–CMP and TBB–BPDA–CMP in FT-IR spectra revealed their successful preparation (Fig. S7A). BET surface area of TBB–DMB–CMP and TBB–BPDA–CMP reached up to 964.02, 965.90  $\text{m}^2\cdot\text{g}^{-1}$  (Fig. S7B and S7C), respectively, and their values were comparable to that of BPT–DMB–CMP ( $1,019.89 \text{ m}^2\cdot\text{g}^{-1}$ ). The adsorption capacities of CQP on BPT–DMB–CMP, TBB–DMB–CMP and TBB–BPDA–CMP were compared, as displayed in Fig. 9. BPT–DMB–CMP with triazine groups has given significantly higher adsorption capacity toward CQP compared with other two CMP without triazine groups. This phenomenon indicated that the multitudinous N-rich functional sites on CMP is conducive to excellent removal performance via potential halogen-bonding interaction.

### 3.7. Real water sample application

To further evaluate practicability of BPT–DMB–CMP for the removal of CQP in actual sample implementation, adsorption regeneration ability was investigated. An acetonitrile solution containing  $\text{NH}_3\cdot\text{H}_2\text{O}$  (5 %) was used to desorb CQP from BPT–DMB–CMP within 10 min of oscillation for a total of three times. Purified water was used as a single wash. The adsorbed CQP was successfully desorbed in an alkaline eluent due to the effect of strong electrostatic repulsive interactions in the desorption process, which could be explained by the zeta potential of BPT–DMB–CMP and the pKa of CQP (in Fig. 2C). After five desorption procedures, the adsorption capacity of BPT–DMB–CMP decreased (see Fig. 10A). This performance confirmed the excellent adsorption regeneration ability of BPT–DMB–CMP for the removal of CQP. BPT–DMB–CMP performed high adsorption capacity for CQP (Fig. 10B and Table S2) at the concentration of 50 and  $100 \text{ mg}\cdot\text{g}^{-1}$  CQP in spiked pharmaceutical factories effluents, pool water, and underground water,

**Table 4**  
Thermodynamic parameters for adsorption of CQP onto BPT-DMB-CMP.

T(°C)	$K_g(\text{kJ}\cdot\text{mol}^{-1})$	$K_c(\text{dimensionless})$	$\Delta G^0(\text{kJ}\cdot\text{mol}^{-1})$	$\Delta H^0(\text{kJ}\cdot\text{mol}^{-1})$	$\Delta S^0(\text{kJ}\cdot\text{mol}^{-1}\cdot\text{K}^{-1})$
25	$4.61 \times 10^3$	$4.61 \times 10^3$	-5.13		
35	$4.65 \times 10^3$	$4.65 \times 10^3$	-6.17	20.12	0.133
45	$2.07 \times 10^3$	$2.07 \times 10^3$	-7.34		

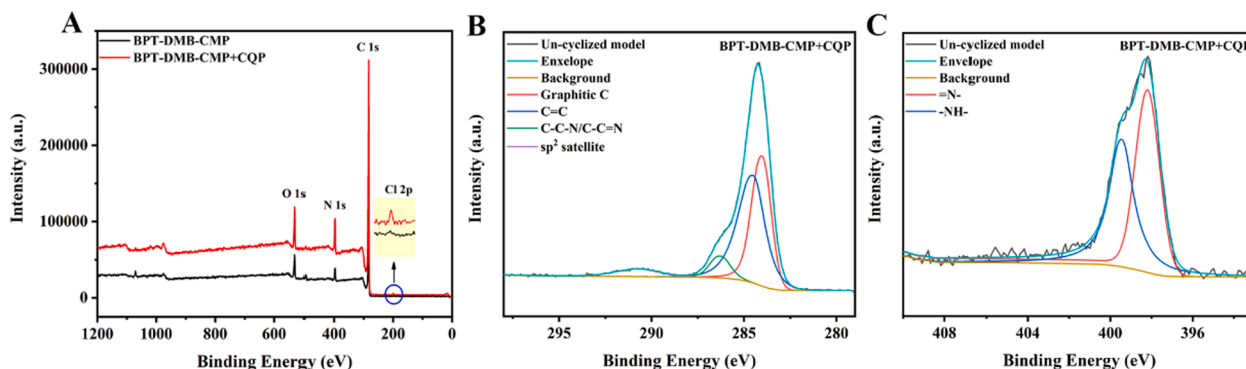


**Fig. 7.** (A) The XPS of full scan of BPT-DMB-CMP before and after CQP adsorption, the XPS of (B) C 1s and (C) N 1s of BPT-DMB-CMP after CQP adsorption.

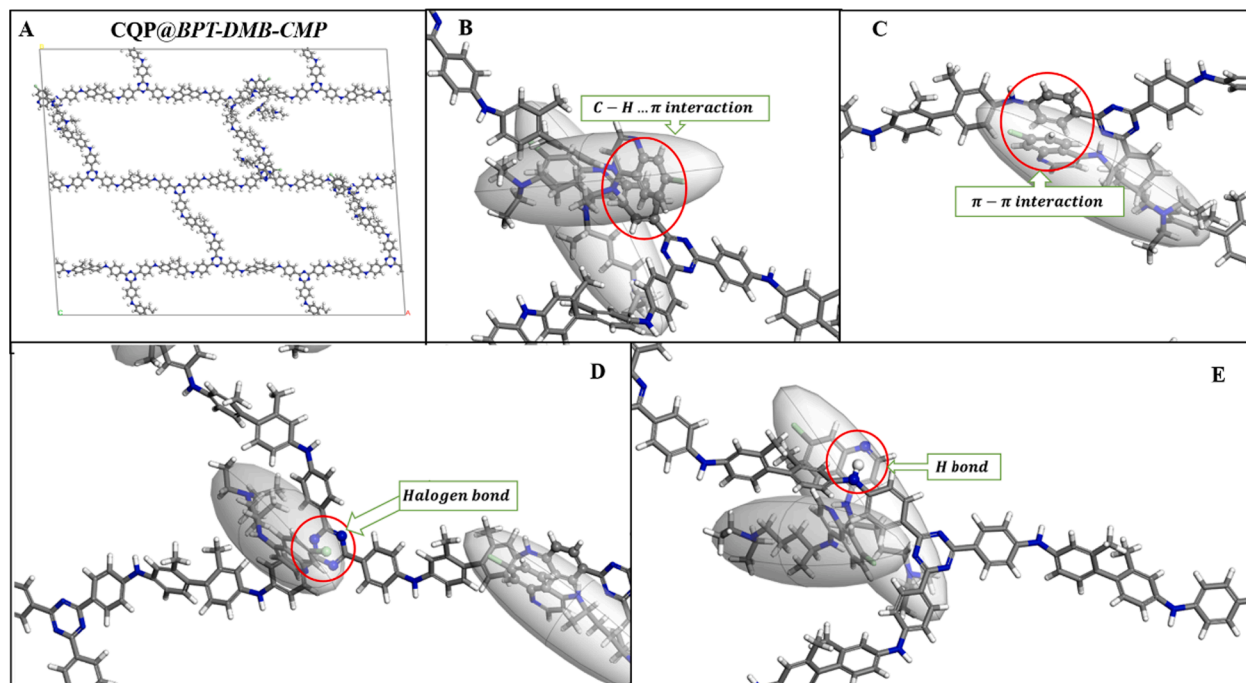


**Fig. 8.** (A) Optimized configurations of 5 molecules of CQP adsorption onto the  $2 \times 2 \times 1$  BPT-DMB-CMP under the top view, and (B, C, D, E) different interactions between CQP and BPT-DMB-CMP.

and results were consistent with the data in purified water. And the removal efficiencies of CQP at the concentration of 50 and  $100 \text{ mg}\cdot\text{g}^{-1}$  CQP in spiked three real wastewater samples ranged from 90.37 % to 99.97 %. The phenomena revealing that the great prospects of BPT-DMB-CMP for adsorption and removal of CQP from wastewater samples. These results showed the potential feasibility of BPT-DMB-CMP as an outstanding adsorbent for practical application.

### 3.8. Evaluation of adsorption capacities for other antiviral drugs

In order to further open up the potential application of BPT-DMB-CMP for other contaminants, the adsorption capacities of BPT-DMB-

CMP towards antiviral drugs such as famciclovir, lamivudine, and favipiravir with similar structures and high water-solubility to CQP were estimated (Table 5). The studied concentration of each antiviral drug in single system was  $100 \text{ mg}\cdot\text{L}^{-1}$ . The structure properties and the differences of adsorption capacities of antiviral drugs on BPT-DMB-CMP adsorbent were displayed in Table 5. All antiviral drugs exhibited relatively high adsorption on BPT-DMB-CMP, revealing the pivotal role of hydrogen or halogen bonding interactions and the potential universality of BPT-DMB-CMP in acquiring high effective adsorption and removal of antiviral drugs. In addition, the adsorption capacities of CQP and famciclovir on BPT-DMB-CMP were higher than those of lamivudine, and favipiravir, and this is likely due to size-matching effect. To sum up, the

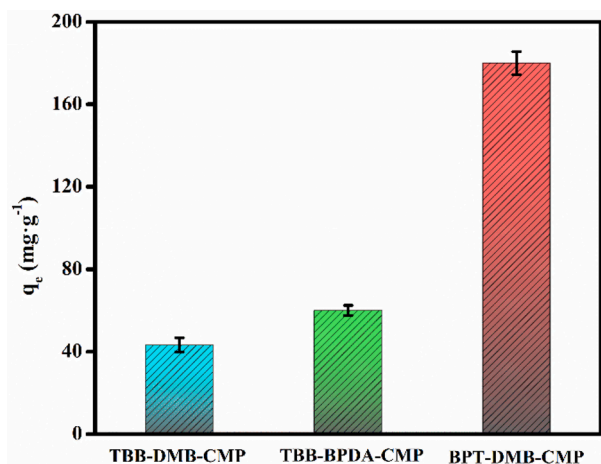


Fig. 9. Comparison of adsorption capacity of CQP on TBB-DMB-CMP, TBB-BPDA-CMP and BPT-DMB-CMP at 308 K with the concentration 100 mg/L.

adsorption performance of antiviral drugs on BPT-DMB-CMP involved multiple interactions of functional groups and molecular size.

The high-effectiveness evaluation of competitive adsorption behavior of multiple pollutants on adsorbent in mixed system will offer

significant guides in practical application. Herein, the competitive adsorption test of CQP, famciclovir, lamivudine, and favipiravir on BPT-DMB-CMP was conducted under same concentration of 100 mg·L<sup>-1</sup>. As shown in Fig. S8, compared to adsorption performances in single system, the adsorption capacities of CQP, famciclovir, lamivudine, and favipiravir on BPT-DMB-CMP decreased to 122.23, 137.26, 36.12, 46.45 mg·g<sup>-1</sup>, demonstrating the poor selectivity of BPT-DMB-CMP for antiviral drugs contaminants. The above result was due to the occurrence of competitive adsorption for the active adsorption sites on adsorbents. Thus, this competitive adsorption among the multiple pollutants should be explored in real application.

#### 4. Conclusions

In conclusion, the C–N bond linked BPT-DMB-CMP was firstly prepared and applicable to efficiently adsorb and remove CQP from aqueous solutions as a water treatment measure. According to the results of the theoretical simulations and XPS characterizations, the method is promising. With the introduction of abundant and rich N–H bonds, triazine rings, and benzene rings in conjunction with the CMP's superb properties (including large surface area of 1,019.89 m<sup>2</sup>·g<sup>-1</sup>), multiple adsorption sites were created via the driving forces of halogen bonding, hydrogen bonding,  $\pi$ - $\pi$  and C–H... $\pi$  stackings. After exploring the entire adsorption process of CQP onto BPT-DMB-CMP in detail via multiple

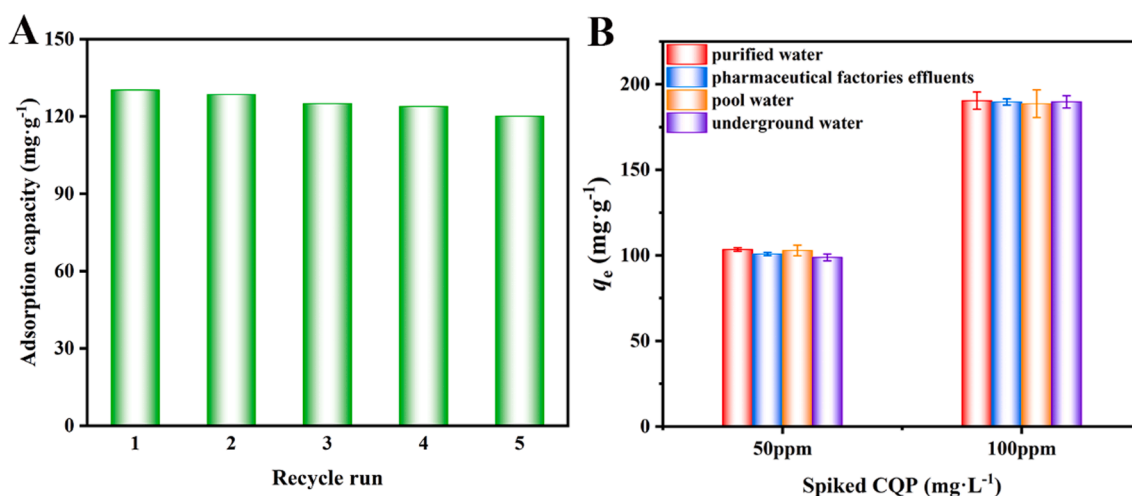
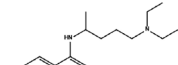
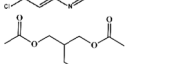
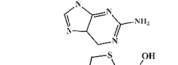
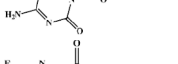


Fig. 10. (A) Effect of elution number on the adsorption capacity of BPT-DMB-CMP under an initial CQP concentration of 100 mg·L<sup>-1</sup>, (B) adsorption of CQP from spiked purified water and real wastewater samples (50 and 100 mg·L<sup>-1</sup>) on BPT-DMB-CMP.

Table 5

Structures properties and adsorption capacity of each antiviral drug on BPT-DMB-CMP adsorbent at 308 K with the concentration 100 mg/L.

Analyte	Structure	<sup>3</sup> H bond acceptors	<sup>1</sup> H bond donors	Halogen bond	<sup>c</sup> Molar volume(cm <sup>3</sup> )	$q_e$ (mg·g <sup>-1</sup> )
CQP		3	1	1	183.6	189.1 ± 3.4
Famciclovir		9	2	0	221.5	194.2 ± 4.8
Lamivudine		6	3	0	132.2	111.5 ± 2.9
Favipiravir		5	3	0	97.2	92.4 ± 6.4

<sup>abc</sup>are obtained from <http://www.chemspider.com>.

kinetics, isotherms, and thermodynamics models, Liu model and MO model were determined to good fits. Good adsorption and removal performance of CQP from three real wastewater samples showed the great prospects of BPT–DMB–CMP for practical application. Meanwhile, with preeminent adsorption ability, BPT–DMB–CMP becomes an excellent candidate adsorbent for removal multiple antiviral drugs. In-depth investigation of adsorption mechanism offers a theoretical guide for building novel highly-efficient adsorbents.

### CRedit authorship contribution statement

**Xiao-Xing Wang:** Methodology, Investigation, Writing – original draft. **Lu Liu:** Conceptualization, Data curation, Validation. **Qi-Feng Li:** Project administration. **Hua Xiao:** Methodology. **Ming-Lin Wang:** Writing - review & editing. **Hai-Chen Tu:** Formal analysis. **Jin-Ming Lin:** Funding acquisition. **Ru-Song Zhao:** Validation, Supervision, Funding acquisition.

### Declaration of Competing Interest

The authors declare that they have no known competing financial interests or personal relationships that could have appeared to influence the work reported in this paper.

### Data availability

Data will be made available on request.

### Acknowledgements

This work was financially supported by the National Natural Science Foundation of China (22076086), Taishan Scholar Program of Shandong Province (ts20190948), Jinan University and Institute Innovation Team Project (2020GXRC008 and 2019GXRC032) and Key Technology R&D Program of Shandong Province (2021ZDSYS12). The authors thank Shiyanjia Lab ([www.shiyanjia.com](http://www.shiyanjia.com)) for the language editing service.

### Appendix A. Supplementary material

Supplementary data to this article can be found online at <https://doi.org/10.1016/j.seppur.2022.122517>.

### References

- [1] D. Bhadra, S. Bhadra, N.K. Jain, PEGylated peptide dendrimeric carriers for the delivery of antimicrobial drug chloroquine phosphate, *Pharm. Res.* 23 (2006) 623–633, <https://doi.org/10.1007/s11095-005-9396-9>.
- [2] S. M. Vouri, T. N. Thai, A. G. Winterstein An evaluation of co-use of chloroquine or hydroxychloroquine plus azithromycin on cardiac outcomes: A pharmacoepidemiological study to inform use during the COVID19 pandemic, *Res. Social. Adm. Pharm.* 17 (2021) 2012–2017. <https://doi.org/10.1016/j.sapharm.2020.04.031>.
- [3] F. Touret, X. de Lamballerie, Lamballerie Of chloroquine and COVID-19, *Antivir. Res.* 177 (2020) 104762.
- [4] C. Cui, M. Zhang, X. Yao, S. Tu, Z. Hou, V. S. Jie En, X. Xiang, J. Lin, T. Cai, N. Shen, C. Song, J. Qiao, S. Zhang, H. Li, D. Liu Dose selection of chloroquine phosphate for treatment of COVID-19 based on a physiologically based pharmacokinetic model, *Acta. Pharm. Sin.* B 10 (2020) 1216–1227. <https://doi.org/10.1016/j.apsb.2020.04.007>.
- [5] J. Gao, Z. Tian, X. Yang, Breakthrough Chloroquine phosphate has shown apparent efficacy in treatment of COVID-19 associated pneumonia in clinical studies, *Biosci. Trends* 14 (2020) 72–73, <https://doi.org/10.5582/bst.2020.01047>.
- [6] S. D. Richardson, S. Y. Kimura Water Analysis: Emerging Contaminants and Current Issues, *Anal. Chem.* 92 (2020) 473–505. <https://doi.org/10.1021/acs.analchem.7b04577>.
- [7] S. D. Richardson, T. A. Ternes Water Analysis: Emerging Contaminants and Current Issues, *Anal. Chem.*, 77 (2005) 3807–3838.
- [8] A. S. Coelho, C. E. P. Chagas, R. M. de Padua, G. A. Pianetti, C. Fernandes A comprehensive stability-indicating HPLC method for determination of chloroquine in active pharmaceutical ingredient and tablets: Identification of oxidation impurities, *J. Pharm. Biomed. Anal.* 145 (2017) 248–254. <https://doi.org/10.1016/j.jpba.2017.06.023>.
- [9] X. H. Yi, H. D. Ji, C. C. Wang, Y. Li, Y. H. Li, C. Zhao, A. Wang, H. F. Fu, P. Wang, X. Zhao, W. Liu Photocatalysis-activated SR-AOP over PDINH/MIL-88A(Fe) composites for boosted chloroquine phosphate degradation: Performance, mechanism, pathway and DFT calculations, *App. Catal. B: Environ.* 293 (2021) 120229–120233. <https://doi.org/10.1016/j.apcatb.2021.120229>.
- [10] F. X. Wang, C. C. Wang, X. D. Du, Y. Li, F. Wang, P. Wang Efficient removal of emerging organic contaminants via photo-Fenton process over micron-sized Fe-MOF sheet, *Chem. Eng. J.* 429 (2022) 132495–132518. <https://doi.org/10.1016/j.cej.2021.132495>.
- [11] X. M. Peng, J. Q. Wu, Z. L. Zhao, X. Wang, H. L. Dai, Y. Wei, G. P. Xu, F. P. Hu Activation of peroxymonosulfate by single atom Co-N-C catalysts for high-efficient removal of chloroquine phosphate via non-radical pathways: Electron-transfer mechanism, *Chem. Eng. J.* 429 (2022) 132245–132258 <https://doi.org/10.1016/j.cej.2021.132245>.
- [12] J. B. Dan, P. H. Rao, Q. F. Wang, M. Zhang, Z. D. He, W. Q. Zhang, N. Y. Gao, J. Deng, J. X. Chen Catalytic performance of wrapped CoO by MgO in oxidative degradation of chloroquine phosphate with peroxymonosulfate, *Appl. Surf. Sci.* 573 (2022) 151430–151442. <https://doi.org/10.1016/j.apsusc.2021.151430>.
- [13] F. M. Kasperiski, E. C. Lima, C. S. Umpierrez, G. S. dos Reis, P. S. Thue, D. R. Lima, S. L. P. Dias, C. Saucier, J. B. da Costa Production of porous activated carbons from Caesalpinia ferrea seed pod wastes: Highly efficient removal of captopril from aqueous solutions, *J. Clean. Prod.* 197 (2018) 919–929. <https://doi.org/10.1016/j.jclepro.2018.06.146>.
- [14] Y. Zhang, K. Pan, Q. Zhong Characteristics of activated carbon and carbon nanotubes as adsorbents to remove annatto (norbixin) in cheese whey, *J. Agric. Food. Chem.* 61 (2013) 9230–9240. <https://doi.org/10.1021/jf402537y>.
- [15] Y. Lv, J. Ma, K. Liu, Y. Jiang, G. Yang, Y. Liu, C. Lin, X. Ye, Y. Shi, M. Liu, L. Chen Rapid elimination of trace bisphenol pollutants with porous beta-cyclodextrin modified cellulose nanofibrous membrane in water: adsorption behavior and mechanism, *J. Hazard. Mater.* 403 (2021) 123666–123680. <https://doi.org/10.1016/j.jhazmat.2020.123666>.
- [16] E. K. Putra, R. Pranowo, J. Sunarso, N. Indraswati, S. Ismadij Performance of activated carbon and bentonite for adsorption of amoxicillin from wastewater: mechanisms, isotherms and kinetics, *Water Res.* 43 (2009) 2419–2430. <https://doi.org/10.1016/j.watres.2009.02.039>.
- [17] L. Li, F. Liu, X. Jing, P. Ling, A. Li Displacement mechanism of binary competitive adsorption for aqueous divalent metal ions onto a novel IDA-chelating resin: isotherm and kinetic modeling, *Water Res.* 45 (2011) 1177–1188. <https://doi.org/10.1016/j.watres.2010.11.009>.
- [18] E. Gagliano, M. Sgroi, P. P. Falciglia, F. G. A. Vagliasindi, P. Roccaro Removal of poly- and perfluoroalkyl substances (PFAS) from water by adsorption: Role of PFAS chain length, effect of organic matter and challenges in adsorbent regeneration, *Water Res.* 171 (2020) 115381–115412. <https://doi.org/10.1016/j.watres.2019.115381>.
- [19] H. Y. Niu, D. Zhang, Z. F. Meng, Y. Q. Cai Fast defluorination and removal of norfloxacin by alginate/Fe@Fe3O4 core/shell structured nanoparticles, *J. Hazard. Mater.* 227–228 (2012) 195–203. <https://doi.org/10.1016/j.jhazmat.2012.05.036>.
- [20] J. C. Zhang, L. Qin, Y. Z. Yang, X.G. Liu Porous carbon nanospheres aerogel based molecularly imprinted polymer for efficient phenol adsorption and removal from wastewater, *Sep. Purif. Technol.* 274 (2021) 119029–119038. <https://doi.org/10.1016/j.seppur.2021.119029>.
- [21] L. X. Zhao, H. Xiao, M. H. Li, M. Xie, N. Li, R. S. Zhao Effectively removing indole-3-butyric acid from aqueous solution with magnetic layered double hydroxide-based adsorbents, *J. Hazard. Mater.* 408 (2021) 124446–124456. <https://doi.org/10.1016/j.jhazmat.2020.124446>.
- [22] S. Zhuang, R. Chen, Y. Liu, J. Wang Magnetic COFs for the adsorptive removal of diclofenac and sulfamethazine from aqueous solution: Adsorption kinetics, isotherms study and DFT calculation, *J. Hazard. Mater.* 385 (2020) 121596–121604. <https://doi.org/10.1016/j.jhazmat.2019.121596>.
- [23] X. X. Fu, P. Wang, J. D. Wu, P. Y. Zheng, T. T. Wang, X. X. Li, M. Z. Ren Hydrocotyle vulgaris derived novel biochar beads for phosphorus removal: static and dynamic adsorption assessment, *J. Environ. Chem. Eng.*, 10 (2022) 108177–108187. <https://doi.org/10.1016/j.jece.2022.108177>.
- [24] L. Feng, C. Zhu, H. Yuan, L. Liu, F. Lv, S. Wang Conjugated polymer nanoparticles: preparation, properties, functionalization and biological applications, *Chem. Soc. Rev.* 42 (2013) 6620–33. <https://doi.org/10.1039/C3CS60036J>.
- [25] Y. Xu, S. Jin, H. Xu, A. Nagai, D. Jiang Conjugated microporous polymers: design, synthesis and application, *Chem. Soc. Rev.* 42 (2013) 8012–8031. <https://doi.org/10.1039/C3CS60160A>.
- [26] P. Johannes, M. Stefan Nanoparticles of Conjugated Polymers, *Chem. Rev.* 110 (2010) 6260–6279. <https://doi.org/10.1021/cr100132y>.
- [27] J. M. Lee, A. I. Cooper Advances in Conjugated Microporous Polymers, *Chem. Rev.* 120 (2020) 2171–2214. <https://doi.org/10.1021/acs.chemrev.9b00399>.
- [28] W. J. Zhang, Q. Peng, H. Yang, Z. J. Fang, J. Y. Deng, G. P. Yu, Y. F. Liao, S. Z. Liao, Q. Q. Liu Modulating Carrier Transfer over Carbazolic Conjugated Microporous Polymers via Donor Structural Design for Functionalization of Thiophenols, *ACS Appl. Mater. Interfaces* 13 (2021) 60072–60083. <https://doi.org/10.1021/acsami.1c20579>.
- [29] Z.Z. Deng, H.W. Zhao, X.X. Cao, S.H. Xiong, G. Li, J.Y. Deng, H. Yang, W.J. Zhang, Q.Q. Liu, Enhancing built-in electric field via molecular dipole control in conjugated microporous polymers for boosting charge separation, *ACS Appl. Mater. Interfaces* 14 (2022) 35745–35754, <https://doi.org/10.1021/acsami.2c08747>.
- [30] W. J. Zhang, Z. Z. Deng, J. Y. Deng, C. T. Au, Y. F. Liao, H. Yang, Q. Q. Liu Regulating the exciton binding energy of covalent triazine frameworks for

- enhancing photocatalysis. *J. Mater. Chem. A* (2022). <https://doi.org/10.1039/D2TA06479K>.
- [31] S. J. Yang, X. S. Ding, B. H. Han Conjugated Microporous Polymers with Extended  $\pi$ -Structures for Organic Vapor Adsorption, *Macromolecules* 51 (2018) 947–953. <https://doi.org/10.1021/acs.macromol.7b02515>.
- [32] C. Zhu, L. Liu, Q. Yang, F. Lv, S. Wang Water-soluble conjugated polymers for imaging, diagnosis, and therapy, *Chem. Rev.* 112 (2012) 4687–4735. <https://doi.org/10.1021/cr200263w>.
- [33] J. X. Jiang, F. Su, A. Trewin, C. D. Wood, H. Niu, J. T. A. Jones, Y. Z. Khimyak, A. I. Cooper Synthetic Control of the Pore Dimension and Surface Area in Conjugated Microporous Polymer and Copolymer Networks, *J. Am. Chem. Soc.* 130 (2008) 7710–7720. <https://doi.org/10.1021/ja8010176>.
- [34] Y. Liao, J. Weber, B. M. Mills, Z. Ren, C. F. J. Faul Highly Efficient and Reversible Iodine Capture in Hexaphenylbenzene-Based Conjugated Microporous Polymers, *Macromolecules* 49 (2016) 6322–6333. <https://doi.org/10.1021/acs.macromol.6b00901>.
- [35] L. Pan, Z. Liu, M. Tian, B. C. Schroeder, A. E. Aliev, C. F. J. Faul Luminescent and Swellable Conjugated Microporous Polymers for Detecting Nitroaromatic Explosives and Removing Harmful Organic Vapors, *ACS Appl. Mater. Interfaces* 11 (2019) 48352–48362. <https://doi.org/10.1021/acsami.9b16767>.
- [36] H. Zhang, L. Zhong, J. Xie, F. Yang, X. Liu, X. Lu A COF-Like N-Rich Conjugated Microporous Polytriphenylamine Cathode with Pseudocapacitive Anion Storage Behavior for High-Energy Aqueous Zinc Dual-Ion Batteries, *Adv. Mater.* 33 (2021) 2101857–2101866. <https://doi.org/10.1002/adma.202101857>.
- [37] X. Sheng, H. Shi, L. Yang, P. Shao, K. Yu, X. Luo Rationally designed conjugated microporous polymers for contaminants adsorption, *Sci. Total. Environ.* 750 (2021) 141683–141699. <https://doi.org/10.1016/j.scitotenv.2020.141683>.
- [38] Y. Liao, H. Wang, M. Zhu, A. Thomas Efficient Supercapacitor Energy Storage Using Conjugated Microporous Polymer Networks Synthesized from Buchwald-Hartwig Coupling, *Adv. Mater.* 30 (2018) 1705710–1705720. <https://doi.org/10.1002/adma.201705710>.
- [39] J. Chen, W. Yan, E. J. Townsend, J. Feng, L. Pan, V. Del Angel Hernandez, C. F. J. Faul Tunable Surface Area, Porosity, and Function in Conjugated Microporous Polymers, *Angew. Chem. Int. Ed.* 58 (2019) 11715–11719. <https://doi.org/10.1002/anie.201905488>.
- [40] X. Guo, J., Wang A general kinetic model for adsorption: theoretical analysis and modeling, *J. Mol. Liq.* 288 (2019) 111100–111107. <https://doi.org/10.1016/j.molliq.2019.111100>.
- [41] G. Xu, B. Zhang, X. Wang, N. Li, L. Liu, J.M. Lin, R.s. Zhao, Nitrogen-doped flower-like porous carbon nanostructures for fast removal of sulfamethazine from water, *Environ. Pollut.* 255 (2019) 113229–113237. <https://doi.org/10.1016/j.envpol.2019.113229>.
- [42] L.X. Zhao, J.L. Liang, N. Li, H. Xiao, L.Z. Chen, R.s. Zhao, Kinetic, thermodynamic and isotherm investigations of Cu(2+) and Zn(2+) adsorption on LiAl hydrotalcite-like compound, *Sci. Total. Environ.* 716 (2020) 137120–137129. <https://doi.org/10.1016/j.scitotenv.2020.137120>.
- [43] P.D. Pathak, S.a. Mandavgane, Preparation and characterization of raw and carbon from banana peel by microwave activation: application in citric acid adsorption, *J. Environ. Chem. Eng.* 3 (2015) 2435–2447. <https://doi.org/10.1016/j.jece.2015.08.023>.
- [44] Y.u. Liu, Y.-J. Liu, Biosorption isotherms, kinetics and thermodynamics, *Separation and Purification Technol.* 61 (3) (2008) 229–242.
- [45] E.C. Lima, H.B. Ahmad, M.P. Juan Carlos, I. A, A critical review of the estimation of the thermodynamic parameters on adsorption equilibria. Wrong use of equilibrium constant in the Van't Hoof equation for calculation of thermodynamic parameters of adsorption, *J. Mol. Liq.* 273 (2019) 425–434. <https://doi.org/10.1016/j.molliq.2018.10.048>.
- [46] M.A. Iwuagwu, K.s. Aloko, Adsorption of Paracetamol and Chloroquine Phosphate by Some Antacids, *J. Pharm. Pharmacol.* 44 (1992) 655–658. <https://doi.org/10.1111/j.2042-7158.1992.tb05488.x>.
- [47] A.O. Dada, A.A. Inyinbor, O.S. Bello, B.e. Tokula, Novel plantain peel activated carbon-supported zinc oxide nanocomposites (PPAC-ZnO-NC) for adsorption of chloroquine synthetic pharmaceutical used for COVID-19 treatment, *Biomass Convers. Bior.* (2021). <https://doi.org/10.1007/s13399-021-01828-9>.
- [48] T.B. Deborah, P.O. Abimbola, A. I, Adejumo Acid-activated Hibiscus sabdariffa seed pods biochar for the adsorption of Chloroquine phosphate: prediction of adsorption efficiency via machine learning approach, *South African Journal of, Chemical Eng.* 42 (2022) 162–175. <https://doi.org/10.1016/j.sajce.2022.08.012>.
- [49] C.M.B. de Araujo, G. Wernke, M.G. Ghislandi, A. Diorio, M.F. Vieira, R. Bergamasco, M.A. da Motta Sobrinho, A. Egídio, Rodrigues Continuous removal of pharmaceutical drug chloroquine and Safranin-O dye from water using agar-graphene oxide hydrogel: selective adsorption in batch and fixed-bed experiments, *Environ. Res.* 216 (2023), 114425. <https://doi.org/10.1016/j.envres.2022.114425>.
- [50] C.h. Wu, Adsorption of reactive dye onto carbon nanotubes: equilibrium, kinetics and thermodynamics, *J. Hazard. Mater.* 144 (2007) 93–100. <https://doi.org/10.1016/j.jhazmat.2006.09.083>.
- [51] I.I. Ebralidze, M. Hanif, R. Arjumand, A.A. Azmi, D. Dixon, N.M. Cann, C. M. Crudden, J.H. Horton, Horton solvent induced adhesion interactions between dichlorotriazine films, *J. Phys. Chem. C* 116 (6) (2012) 4217–4223.
- [52] X.Q. He, Y.Y. Cui, C.x. Yang, Thiol-Yne Click Postsynthesis of a sulfonate group-enriched magnetic microporous organic network for efficient extraction of benzimidazole fungicides, *ACS Appl. Mater. Interfaces* 13 (2021) 39905–39914. <https://doi.org/10.1021/acsami.1c11148>.
- [53] X.Q. He, Y.Y. Cui, X.H. Lin, C.x. Yang, Fabrication of polyethyleneimine modified magnetic microporous organic network nanosphere for efficient enrichment of non-steroidal anti-inflammatory drugs from wastewater samples prior to HPLC-UV analysis, *Talanta* 233 (2021) 122471–122482. <https://doi.org/10.1016/j.talanta.2021.122471>.